OPEN ACCESS
OPUS AUGSBURG

Universität Augsburg
Universitätsbibliothek

Signatures of van Hove singularities in the anisotropic in-plane optical conductivity of the topological semimetal Nb3SiTe6

Jihaan Ebad-Allah, Alexander A. Tsirlin, Y. L. Zhu, Z. Q. Mao, Christine A. Kuntscher

Angaben zur Veröffentlichung / Publication details:

Ebad-Allah, Jihaan, Alexander A. Tsirlin, Y. L. Zhu, Z. Q. Mao, and Christine A. Kuntscher. 2023. "Signatures of van Hove singularities in the anisotropic in-plane optical conductivity of the topological semimetal Nb3SiTe6." *Physical Review B* 107 (11): 115115. https://doi.org/10.1103/physrevb.107.115115.

Nutzungsbedingungen / Terms of use: **licgercopyright**

Dieses Dokument wird unter folgenden Bedingungen zur Verfügung gestellt: / This document is made available under these conditions:
Deutsches Urheberrecht
Weitere Informationen finden Sie unter: / For more information see:
https://www.uni-augsburg.de/de/organisation/bibliothek/publizieren-zitieren-archivieren/publiz/

Signatures of van Hove singularities in the anisotropic in-plane optical conductivity of the topological semimetal Nb_3SiTe_6

J. Ebad-Allah,[1,2] A. A. Tsirlin,[3,4] Y. L. Zhu,[5] Z. Q. Mao,[5] and C. A. Kuntscher[1,*]

[1]*Experimentalphysik II, Institute for Physics, University of Augsburg, D-86135 Augsburg, Germany*

[2]*Department of Physics, Tanta University, 31527 Tanta, Egypt*

[3]*Felix Bloch Institute for Solid-State Physics, Leipzig University, 04103 Leipzig, Germany*

[4]*Experimentalphysik VI, Center for Electronic Correlations and Magnetism, Institute for Physics, University of Augsburg, D-86135 Augsburg, Germany*

[5]*Department of Physics, Pennsylvania State University, University Park, Pennsylvania 16802, USA*

(Received 6 October 2022; revised 11 January 2023; accepted 14 February 2023; published 7 March 2023)

We present a temperature-dependent infrared spectroscopy study on the layered topological semimetal Nb_3SiTe_6 combined with density-functional theory calculations of the electronic band structure and optical conductivity. Our results reveal an anisotropic behavior of the in-plane (*ac*-plane) optical conductivity, with three pronounced excitations located at around 0.15, 0.28, and 0.41 eV for the polarization of the incident radiation along the *c* axis. These excitations are well reproduced in the theoretical spectra. Based on the *ab initio* results, the excitations around 0.15 and 0.28 eV are interpreted as fingerprints of van Hove singularities in the electronic band structure and compared to the findings for other topological semimetals.

DOI: 10.1103/PhysRevB.107.115115

I. INTRODUCTION

Novel layered Dirac materials hosting nontrivial band crossings in the vicinity of the Fermi level (E_F) attract considerable attention in condensed-matter research due to their unusual physical properties and phenomena such as anisotropic electron transport [1], chiral anomaly [2], nodal chains [3], hourglass dispersions [4], drumheadlike states [5], van Hove singularities [6–11], and surface superconductivity [12]. The layered ternary telluride compounds M_3SiTe_6 (M = Nb and Ta) are one class of these materials, where the band structure calculations predicted several nontrivial band features near E_F [4,13,14]. Nb_3SiTe_6 is a van der Waals layered material with the crystal structure very similar to that of MoS_2 [15], and can be thinned down to atomically thin two-dimensional (2D) crystals [1,16]. Bulk Nb_3SiTe_6 has an orthorhombic symmetry with the space group *Pnma* [17]. The layers stack via van der Waals forces, forming bundles of sandwich layers with the order Te-(Nb,Si)-Te. Each Te-(Nb,Si)-Te layer is composed of face- and edge-sharing $NbTe_6$ prisms with Si ions inserted into interstitial sites among these prisms, as illustrated in Fig. 1(a). We also depict in Fig. 1(b) the first Brillouin zone of bulk Nb_3SiTe_6 with the high-symmetry points.

In the absence of spin-orbit coupling (SOC), the electronic band structure of M_3SiTe_6 contains (i) a nodal loop related to the linear-band-crossing points along the Γ-Y and Γ-Z paths, and (ii) a fourfold nodal line formed along the S-R path [4,13,14]. Adding SOC leads to several new features, for instance, (i) gapping the nodal loop around the Γ point, (ii) fourfold degeneracy of each band along the paths U-X, R-U, and Z-S, and (iii) the emergence of an hourglass Dirac loop along the S-R path (instead of the nodal line) as well as along S-X. The degeneracies of features (ii) and (iii) result from the nonsymmorphic space-group symmetry. Furthermore, the charge carrier mobility along the a direction was predicted to be much higher due to the Dirac dispersion along this direction, leading to a strong anisotropy in the electronic properties.

Temperature-dependent resistivity measurements on a bulk sample of Nb_3SiTe_6 showed typical metallic behavior with an anisotropy along in-plane and out-of-plane directions, related to the specific bonding state of Nb ions. In particular, according to the projected band structure and density of states the conduction bands crossing the Fermi level are mainly derived from Nb 4*d* orbitals [1]. Furthermore, an in-plane anisotropy is also expected for the M_3SiTe_6 compounds due to the large difference between the in-plane lattice parameters [17]. Consistently, an angle-resolved photoemission spectroscopy study reported a strong anisotropy of the Fermi surface of Ta_3SiTe_6 [13]. In Nb_3SiTe_6, both hole and electron pockets exist, hence, in the bulk the presence of free charge carriers with different scattering rates is expected. The hole-type charge carriers are suggested to prevail in the transport properties of thin flakes [18], while their density will be affected by the deficiency of Te atoms [19].

Despite Nb_3SiTe_6 revealing very interesting electronic properties, its optical conductivity has not been studied yet. In this paper we investigate the temperature-dependent in-plane (*ac*-plane) optical conductivity of bulk Nb_3SiTe_6 single crystal, obtained by frequency-dependent reflectivity measurements for the polarization directions $\mathbf{E}\|a$ and $\mathbf{E}\|c$. The

*christine.kuntscher@physik.uni-augsburg.de

 ©2023 American Physical Society

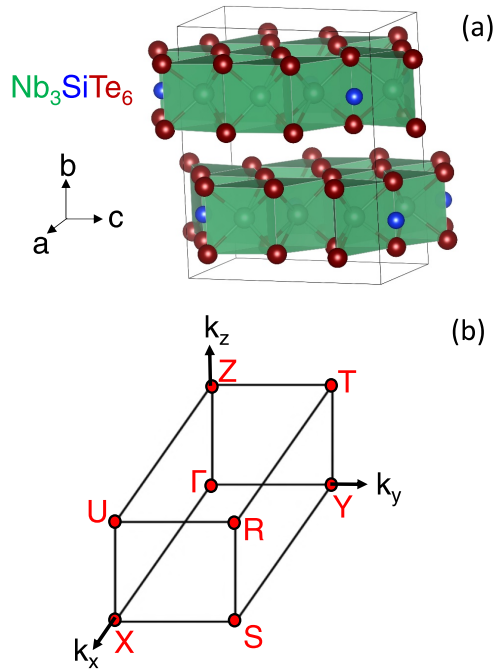

FIG. 1. (a) Crystal structure of Nb_3SiTe_6. (b) First Brillouin zone of Nb_3SiTe_6 with the notation of the high-symmetry points.

optical conductivity shows an anisotropic behavior between the two in-plane polarization directions. Several pronounced interband excitations are observed in the optical conductivity along the c axis, which sharpen as the temperature decreases. Based on density-functional theory (DFT) calculations we relate these excitation peaks to specific transitions between electronic bands and propose that they are related to van Hove singularities in the electronic band structure.

II. SAMPLE PREPARATION AND EXPERIMENTAL DETAILS

Single crystals of Nb_3SiTe_6 were grown using chemical vapor transport with a mixture of Nb, Si, and Te at a molar ratio of 3:1:6. During synthesis, the temperature of the hot and cold ends of the double-zone tube furnace was set at 950 °C and 850 °C, respectively [1,18].

The temperature-dependent reflectivity measurements at ambient pressure were performed between 295 and 6 K in the frequency range from 0.025 to 2.48 eV (200 to 20000 cm^{-1}). Measurements have been conducted on a single crystal on a freshly cleaved $\mathbf{E}\|ac$ surface. A silver layer was evaporated onto half of the sample surface to serve as a reference, and the obtained spectra have been corrected with the mirror reflectivity later on. The sample was mounted on a cold-finger microcryostat. The measurements were carried out for the in-plane polarization directions $\mathbf{E}\|a$ and $\mathbf{E}\|c$ using an infrared microscope (Bruker Hyperion), equipped with a 15× Cassegrain objective, coupled to a Bruker Vertex 80v FT-IR spectrometer.

The Kramers-Kronig (KK) relations were applied to transform the reflectivity spectra into the complex optical conductivity $\sigma(\omega) = \sigma_1(\omega) + i\sigma_2(\omega)$ and the complex dielectric function $\epsilon(\omega) = \epsilon_1(\omega) + i\epsilon_2(\omega)$. The extrapolation of the reflectivity data was done in a manner similar to our previous publications [20–22]. To this end, the reflectivity was extrapolated to low frequencies based on a Drude-Lorentz fit, while for the high-frequency extrapolation we used the x-ray atomic scattering functions [23]. To obtain the contributions to the optical conductivity, the reflectivity and optical conductivity spectra were simultaneously fitted with the Drude-Lorentz model.

The electronic band structure of Nb_3SiTe_6 was calculated in the WIEN2K code [24,25] using the Perdew-Burke-Ernzerhof (PBE) type of the exchange-correlation potential [26]. Lattice parameters and atomic positions from Ref. [27] were employed without further optimization. The corresponding notation of the high-symmetry points is shown in Fig. 1(b). Charge density was converged on the $8 \times 4 \times 4$ k mesh. Consequently, optical conductivity was calculated with the internal routines of WIEN2K [28] on the dense $24 \times 12 \times 12$ mesh.

III. RESULTS AND DISCUSSION

The temperature-dependent reflectivity spectra of Nb_3SiTe_6 for the in-plane polarization directions $\mathbf{E}\|a$ and $\mathbf{E}\|c$ are shown in Figs. 2(a) and 2(b), respectively, and in Fig. S1 in the Supplemental Material [29]. The plasma edge in the reflectivity and the low-frequency reflectivity level, which increases upon cooling and approaches unity at 6 K, both reveal the metallic nature of the compound consistent with transport measurements [1,13,18,19]. The plasma edge in the reflectivity depends not only on the temperature, but also on the polarization direction as illustrated in the inset of Fig. 2(a). Figures 2(c) and 2(d) display the temperature-dependent real part of the optical conductivity σ_1 for both polarization directions, as derived from the reflectivity spectra through KK relations. Corresponding plots on a lin-log scale can be found in Fig. S1 in the Supplemental Material [29]. For both in-plane polarization directions, the σ_1 spectrum shows intraband excitations at low frequencies described by Drude contributions, which become sharper during cooling down due to reduced scattering.

For the further analysis and discussion of other excitations (aside from the intraband transitions) we divide the measured energy range into two regions: (i) the low-energy region (energies between 0.08 and 0.7 eV) and (ii) the high-energy region (energies from 0.7 eV up to 2.25 eV). In the low-energy region, the σ_1 spectrum along both axes shows a drop at around 0.1 eV followed by several polarization-dependent interband excitations at energies below 0.7 eV. Interestingly, most of the observed excitations in this energy range hardly shift with decreasing temperature but only sharpen. This temperature evolution of the low-energy excitations can be explained by a simple approach taking the temperature dependence of the Fermi-Dirac distribution function into account, causing a sharpening of the low-energy interband transitions with cooling. This approach was recently demonstrated for the Weyl semimetal TaP [30]. In the high-energy region, σ_1 exhibits a monotonic increase with increasing frequency overlaid with various excitations, whose positions depend on the polarization direction. The overall changes in the optical conductivity in this energy region during cooling down are modest for both a and c axes.

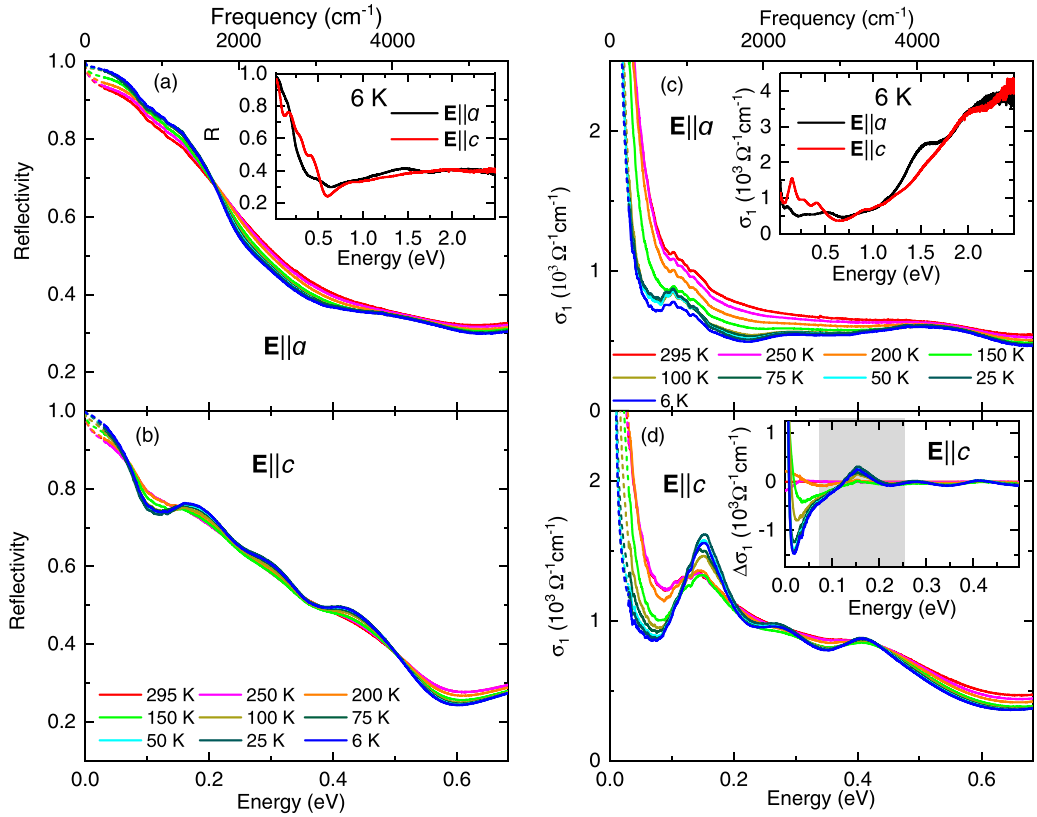

FIG. 2. Temperature-dependent reflectivity spectra of Nb_3SiTe_6 for the polarization directions (a) $\mathbf{E}\|a$ and (b) $\mathbf{E}\|c$. Inset of (a): comparison between the reflectivity spectra at 6 K for the two polarization directions over a broad frequency range. (c), (d) Temperature-dependent optical conductivity σ_1 spectra of Nb_3SiTe_6 for $\mathbf{E}\|a$ and $\mathbf{E}\|c$, respectively. Inset of (c): comparison between the σ_1 spectra at 6 K for the two polarization directions in the entire measured range. Inset of (d): difference spectra $\Delta\sigma_1$ calculated according to $\Delta\sigma_1(\omega, T) = \sigma_1(\omega, T) - \sigma_1(\omega, 295\ \mathrm{K})$. The gray area marks the full-width at half-maximum of the L1 peak at 295 K.

Focusing on the experimental spectra at the lowest studied temperature 6 K, one observes that the optical response contains several pronounced contributions for $\mathbf{E}\|c$ compared to $\mathbf{E}\|a$, as illustrated in the insets of Figs. 2(a) and 2(c). In order to distinguish the optical contributions of each axis, we fitted the σ_1 spectra (and simultaneously the reflectivity spectra) using the Drude-Lorentz model. As an example, we display in the two panels of Fig. 3 the fitting of the σ_1 spectrum together with the fitting contributions for $\mathbf{E}\|a$ and $\mathbf{E}\|c$ at 6 K (see also Figs. S2 and S3 in the Supplemental Material [29]). From the fitting we obtained the following contributions for the polarization $\mathbf{E}\|c$: (i) Below 0.7 eV, the σ_1 spectrum consists of two Drude contributions related to the itinerant charge carriers [19]. The presence of different types of free carriers is reasonable according to the reported electronic band structure, as already mentioned in the Introduction. In fact, two Drude components had to be included in the model for the $\mathbf{E}\|c$ polarization direction to obtain a reasonable fit quality. Most interestingly, the $\mathrm{E}\|c$ σ_1 spectrum shows a sharp peaklike excitation (L1) at around 0.15 eV, followed by two less sharp but still pronounced excitations at around 0.28 and 0.41 eV (L2 and L3, respectively), and a shoulder (L4) at around 0.49 eV. The main interband contributions (L1–L3) to the $\mathbf{E}\|c$ optical conductivity are also highlighted in Fig. 5(c). (ii) Above 0.7 eV, another three high-energy excitations overlay the monotonic increase, and are positioned at approximately 0.93, 1.5, and 2.0 eV [see Fig. 3(b)].

For the polarization direction $\mathbf{E}\|a$ [see Fig. 3(a)], one Drude term was sufficient for obtaining a good fit quality. However, for consistency reasons, we included two Drude contributions for this polariziation direction as well, like for the $\mathbf{E}\|c$ optical spectrum, accounting for different types of carriers. The observed interband excitations below 0.7 eV are smeared out compared to $\mathbf{E}\|c$. In addition, most of the observed excitations below and above 0.7 eV are located at slightly different energies, namely, at around 0.12, 0.29, 0.41, and 0.52 eV in the low-energy region, and at around 0.9, 1.5, and 2.2 eV in the high-energy region [see Fig. 3(a) for the fitting contributions]. These differences between the observed excitations for the two directions give a clear evidence for the in-plane anisotropy of Nb_3SiTe_6, consistent with the in-plane anisotropy of the crystal structure, which is further illustrated by the large difference between the in-plane lattice parameters a and c ($a = 6.353$ Å, $b = 11.507$ Å, $c = 13.938$ Å according to Ref. [27]). An in-plane anisotropy was also observed in the Fermi surface of the sister compound Ta_3SiTe_6 [13].

The in-plane anisotropy is also revealed by the effective plasma frequency ω_p, which was calculated from the plasma frequencies ω_{p1} and ω_{p2} of the two Drude contributions

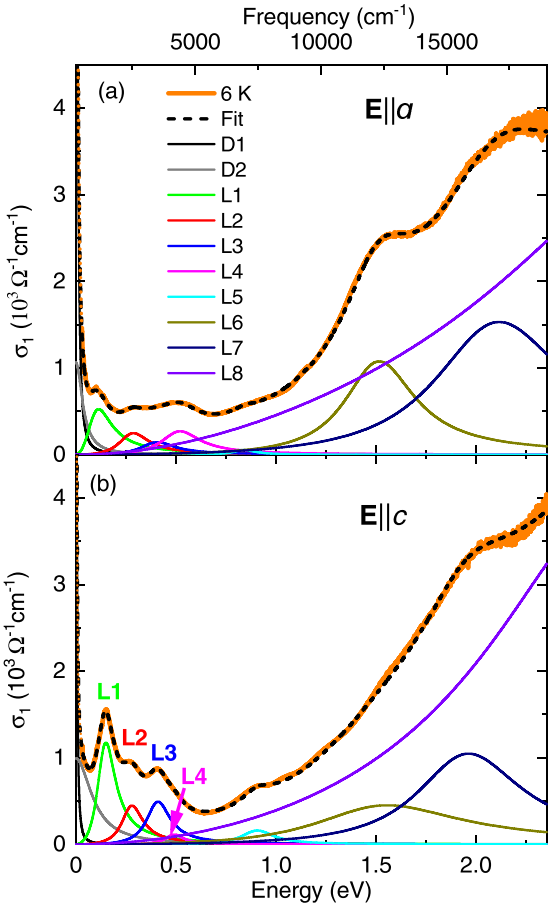

FIG. 3. Real part of the optical conductivity σ_1 of Nb_3SiTe_6 at 6 K for (a) $\mathbf{E}\|a$ and (b) $\mathbf{E}\|c$ together with the total Drude-Lorentz fit and the various fitting contributions (D: Drude term, L: Lorentz term).

according to $\omega_p = \sqrt{\omega_{p1}^2 + \omega_{p2}^2}$. The temperature-dependent plasma frequency for the two measured polarization directions is shown in Fig. 4. For $\mathbf{E}\|a$, ω_p decreases as the temperature decreases, namely, from $\omega_{p,300\,\mathrm{K}} = 1.18$ eV to $\omega_{p,6\,\mathrm{K}} = 1.09$ eV. Such a temperature dependence is expected for a semimetal, with less free carriers at low temperatures [31]. Along the c axis, ω_p exhibits an unusual behavior, where it slightly increases from $\omega_{p,300\,\mathrm{K}} = 1.05$ eV to $\omega_{p,6\,\mathrm{K}} = 1.11$ eV upon cooling (see Fig. 4). Generally, a direct relation should be expected between the electronic kinetic energy and the Drude spectral weight, which is directly proportional to ω_p^2. An increase in ω_p with cooling thus indicates an increase in electronic kinetic energy, which can be due to reduced electron correlation effects, i.e., reduced effective electronic mass [32,33]. Another possible reason could be a temperature-induced shift of the Fermi level, as was recently demonstrated for the semimetal $ZrTe_5$ [34]. However, a Fermi level shift should affect the plasma frequency for both polarization directions in the same manner, which is inconsistent with our results.

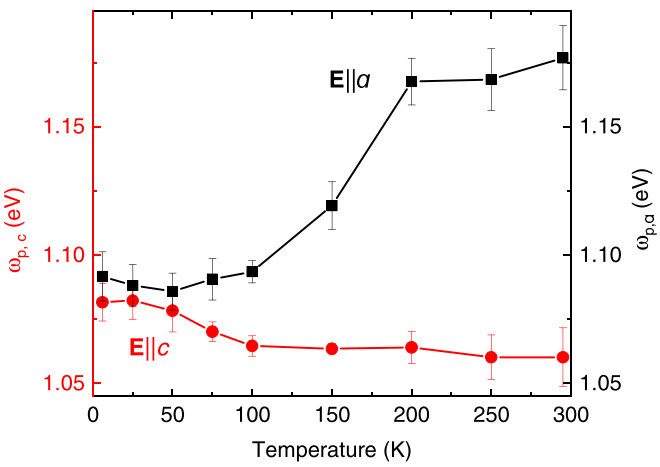

FIG. 4. Temperature-dependent effective plasma frequency of Nb_3SiTe_6 for the polarization directions $\mathbf{E}\|a$ ($\omega_{p,a}$) and $\mathbf{E}\|c$ ($\omega_{p,c}$).

The temperature-dependent σ_1 spectrum for $\mathbf{E}\|c$ suggests a considerable redistribution of the spectral weight from low to high frequencies upon cooling [see Fig. 2(d)]. The difference spectra $\Delta\sigma_1$, defined as $\Delta\sigma_1(\omega, T) = \sigma_1(\omega, T) - \sigma_1(\omega, 295\,\mathrm{K})$, illustrate the temperature-induced reshuffling of the spectral weight among various contributions. Such kind of analysis is in particular interesting for the $\mathbf{E}\|c$ optical conductivity spectrum with the most pronounced excitations. We observe that the spectral weight redistribution mainly occurs between the Drude contributions and the mid-infrared excitations [see inset of Fig. 2(d)]. At first sight, it seems that some Drude spectral weight is transferred to the L1 excitation during cooling down. However, when taking into account the full-width at half-maximum of the L1 peak at room temperature, as indicated by the gray area, it is clear that the spectral weight of the L1 peak is decreased in certain energy ranges during cooling. For better illustration, we plot in Fig. S4 in the Supplemental Material [29] the difference spectra $\Delta\sigma_1$ together with the temperature-dependent L1 Lorentz peak. From our detailed fitting analysis of the experimental data we find that the Drude spectral weight is slightly increasing with decreasing temperature (increasing plasma frequency ω_p for $\mathbf{E}\|c$, see Fig. 4), whereas the spectral weight of the L1 peak (as well as the L2 peak) is decreasing, as will be discussed in more detail later. The transfer of the spectral weight indicates the reconstruction of the electronic bands over the energy range below 0.7 eV.

For the interpretation of the observed excitations in the experimental optical conductivity spectra, we carried out DFT electronic band structure calculations and calculations of the optical conductivity. Hereby, SOC was taken into account. The calculated electronic band structure, as depicted in Fig. 5(b), is in agreement with earlier results [4]. Namely, we observe the gapping of the nodal loop around Γ point, the appearance of an hourglass Dirac loop along the *S*-*R* and *S*-*X* paths, and the degeneracy of the bands along several paths. The electronic band structure contains several nontrivial bands near E_F, mainly originating from Nb 4*d* orbitals [1], as evidenced by the partial density of states depicted in Fig. 6(b). For the further discussion, we group adjacent electronic bands into pairs, labeled A, B, C, and D, with the C and D bands lying in direct vicinity of E_F. The theoretical plasma frequencies from the DFT calculations amount to 0.138 eV for $\mathbf{E}\|a$, 0.699 eV for $\mathbf{E}\|b$, and 0.943 eV for $\mathbf{E}\|c$. Accordingly, the one

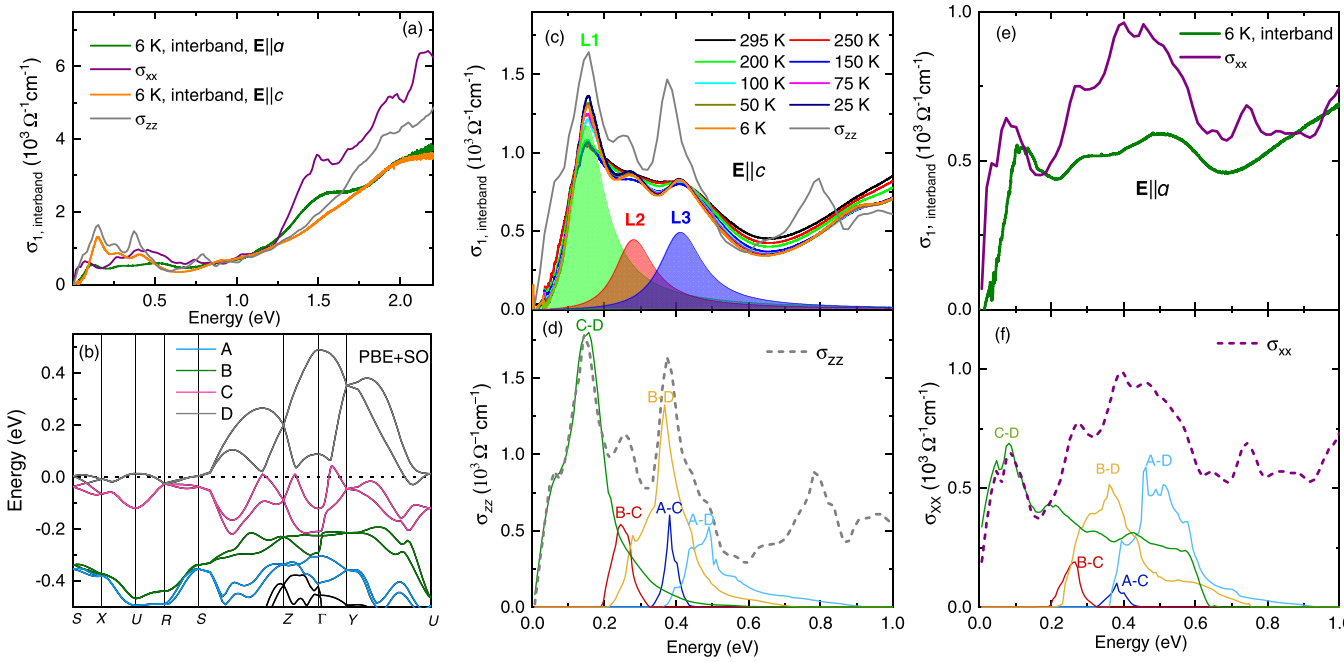

FIG. 5. (a) Comparison between the experimental and DFT interband conductivity $\sigma_{1,\text{interband}}$ for energies up to 2.2 eV for the polarization directions $\mathbf{E}\|a$ and $\mathbf{E}\|c$ at 6 K. (b) Calculated electronic band structure of Nb_3SiTe_6 with SOC. (c) Temperature-dependent experimental interband conductivity $\sigma_{1,\text{interband}}$ below 1.0 eV for the polarization directions $\mathbf{E}\|c$ compared with the DFT interband conductivity σ_{zz}. The colored peaks are the fitting contributions for L1, L2, L3 using the Lorentz model. (d) Contributions of different band combinations to the optical conductivity σ_{zz}. (e) The experimental $\sigma_{1,\text{interband}}$ at 6 K for the polarization $\mathbf{E}\|a$ compared with the DFT interband conductivity σ_{xx}. (f) Contributions of different band combinations to the optical conductivity σ_{xx}.

for $\mathbf{E}\|c$ matches the experimental value, while the one for $\mathbf{E}\|a$ is lower compared to the experimental result.

Figure 5(a) displays a comparison between the calculated interband conductivity σ_{xx} and σ_{zz} together with the corresponding experimental results $\sigma_{1,\text{interband}}$ at 6 K for the polarization directions $\mathbf{E}\|a$ and $\mathbf{E}\|c$, respectively, over a broad energy range. As DFT provides only the interband contribution, we subtracted the Drude terms from the experimental σ_1 spectra and show $\sigma_{1,\text{interband}}$. Obviously, the overall experimental interband conductivity spectra for both polarization directions are well reproduced by theory, especially in the low-energy region below 1 eV, which will be the main focus in the following. The somewhat less favorable agreement above 1 eV is probably caused by inaccuracies in the description

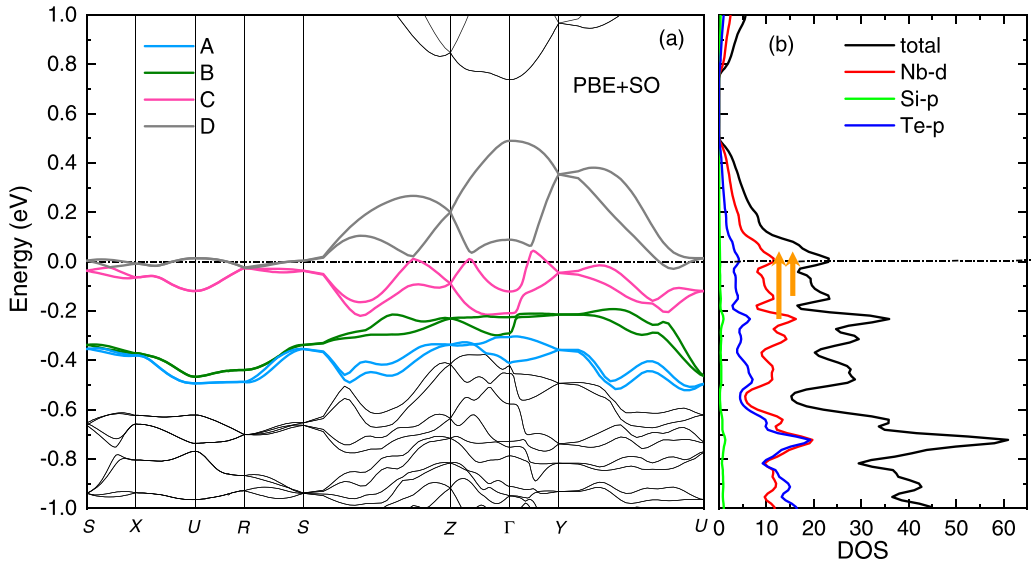

FIG. 6. (a) Calculated electronic band structure of Nb_3SiTe_6. (b) Total density of states together with the partial density of states for Nb $4d$, Si $3p$, and Te $5p$. The two vertical arrows mark the possible electronic transitions, which could explain the two low-frequency absorption peaks L1 and L2 in the $\mathbf{E}\|c$ optical conductivity.

of the excited states within DFT. It is important to note that the agreement between theory and experiment is in particular obvious for the $\mathbf{E}\|c$ polarization direction since the theoretical σ_{zz} spectrum also shows a low-energy three-peak profile with peak energies 0.15, 0.26, and 0.38 eV, corresponding to the L1, L2, and L3 peaks at positions 0.15, 0.28, and 0.41 eV in the measured σ_1 spectrum.

The calculated optical conductivity reveals a tiny peak below 0.1 eV for both polarization directions, which is absent in the experimental spectra and most likely hidden behind the Drude contribution. This tiny peak might be due to transitions within the hourglass Dirac loop very close to E_F. One furthermore observes that the experimental $\mathbf{E}\|c$ $\sigma_{1,\text{interband}}$ below the first sharp L1 excitation is approximately linear in frequency and temperature independent, although the L1 peak itself shows a significant temperature dependence in its intensity. A similar behavior was recently observed for the nodal-line semimetal $BaNiS_2$ [35]. Here, temperature-dependent peaks in the theoretical optical conductivity spectra, located at the high-energy limit of a temperature-independent isosbestic linear-in-frequency conductivity, were associated with van Hove singularities (vHS's). These vHS's are related to saddle points of the electronic bands which result from the connections between Dirac cones in the reciprocal space. Although the sharp peaks were not fully developed in the experimental optical data of $BaNiS_2$, it was suggested that such sharp vHS's in σ_1 are signatures of open Dirac nodal lines [35]. In case of $BaNiS_2$ a pronounced transfer of the spectral weight from the Drude contributions to the sharp peaks via the temperature-independent isosbestic line was observed during cooling down, in contrast to our findings. It is important to note that the appearance of a vHS is not a generic feature of open Dirac nodal lines. For example, for dispersive open Dirac nodal lines the linear-in-frequency conductivity may end with a flat spectral response without any noticeable peaks [36,37].

The presence of Dirac nodal lines or loops with corresponding two-dimensional Dirac electrons is expected to cause characteristic fingerprints in the optical response, namely, a frequency-independent interband optical conductivity related to the transitions within the Dirac cones [36,38,39]. It was furthermore shown that energy-dispersive nodal lines (in contrast to flat nodal lines) can cause a linear-in-frequency behavior in the optical conductivity, similar to semimetals with separate Dirac nodal points [37]. As mentioned in the Introduction, the electronic band structure of Nb_3SiTe_6 contains several nodal lines and loops in the vicinity of E_F. However, these nontrivial features are neither revealed in the experimental nor in the theoretical interband conductivity spectra [see Fig. 5(a)].

Based on the DFT calculations we can decompose the interband optical conductivity into contributions of different band combinations. In Figs. 5(d) and 5(f) we display the contributions of the interband transitions C-D, B-C, B-D, A-C, and A-D to the theoretical conductivity spectra σ_{zz} and σ_{xx}, respectively. In the following, we will focus on understanding the origin of these excitations and relate them to the observed excitation features in $\sigma_{1,\text{interband}}$.

By using the Drude-Lorentz fit, we managed to separate each contribution to the experimental σ_1 spectrum and to follow the respective temperature dependence. A direct comparison between the fitting components L1, L2, L3, and L4 in the experimental $\sigma_{1,\text{interband}}$ spectra and the C-D, B-C, B-D, A-C and A-D excitations in the theoretical spectra reveals the following: (i) For $\mathbf{E}\|c$, the sharpest peak L1 originates from transitions between the C-D bands [Figs. 5(c) and 5(d)]. The L2 peak is due to transitions between the B-C bands, while the L3 peak results from transitions between A-C and B-D bands. The shoulder [Lorentz contribution L4, see Fig. 3(b)] above the L3 peak can be associated with A-D transitions. However, based on the results of the DFT calculations we could not locate unique positions in momentum space, where the transitions take place. (ii) For $\mathbf{E}\|a$, the lowest-energy peak can be attributed to C-D transitions, like for $\mathbf{E}\|c$ [see Figs. 5(e) and 5(f)]. However, the interpretation of the higher-energy contributions to $\mathbf{E}\|a$ $\sigma_{1,\text{interband}}$ is less straightforward since the C-D transitions contribute spectral weight over a rather broad frequency range, namely up to 0.6 eV, hence overlaying the contributions of other band combinations B-C, B-D, etc.

Further insight into the origin of these spectral features can be obtained from the electronic density of states (DOS) shown in Fig. 6(b). Two DOS peaks located below the Fermi level manifest vHS's. Another vHS is located right above E_F. The accumulation of electronic states around these energies and the transitions between them [see arrows in Fig. 6(b)] could cause absorption peaks at energies 0.15 and 0.25 eV, which match the energy positions of the first two low-energy peaks in σ_{zz}, and hence could serve as an explanation for the L1 and L2 peaks in the experimental σ_1 spectrum [see Fig. 5(c)]. On the other hand, the fact that no DOS peak accompanies the higher-energy σ_{zz} peaks (and thus L3 and L4) suggests a different origin of these features.

As we mentioned above, the L1, L2, and L3 excitations get sharper on decreasing temperature, while their energy positions are almost frequency independent. Thus, by comparing the temperature dependence of the scattering rate (width) and oscillator strength of these three excitations we can gain insight whether these excitations have the same origin or not. In Figs. 7(a) and 7(b) we display the temperature-dependent scattering rate and oscillator strength, as extracted from the Drude-Lorentz fittings. The L3 excitation shows a different behavior compared to L1 and L2: whereas its width is hardly affected (slight narrowing) during cooling down, its oscillator strength monotonically increases with decreasing temperature and saturates below 100 K. This suggests that the L3 excitation has a different origin than the L1 and L2 excitations. Interestingly, both L1 and L2 excitations display a very similar temperature behavior: below 250 K their width as well as the oscillator strength monotonically decrease down to 100 K. The reduction in the width can be related to the reduced occupation of the bands D that lie immediately above E_F and become less populated when temperature decreases. Below 100 K, both the scattering rate and oscillator strength for the L1 and L2 excitations are approximately constant. Since the L1 and L2 excitations show a similar temperature dependence, we conclude that they have a similar origin, contrasted with L3. This analysis underpins our assignment of L1 and L2 to the vHS features of the band structure.

The vHS interpretation of the L1 and L2 excitations is further supported by the low-dimensional character of the

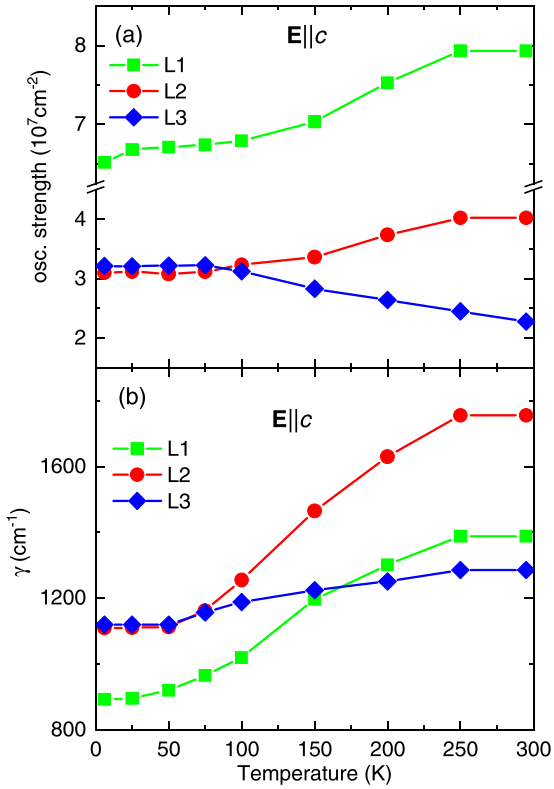

FIG. 7. Temperature-dependent (a) oscillator strength and (b) width (γ) of L1, L2, and L3 excitations for the polarization $\mathbf{E}\|c$, obtained from Drude-Lorentz fittings of σ_1.

material, which leads to an increasing probability for the existence of vHS's in the electronic band structure, like in the layered Dirac semimetal $ZrTe_5$ [6]. Additionally, the observed transfer of the spectral weight upon cooling, combined with the temperature-independent behavior of $\sigma_{1,\text{interband}}$ at energies below L1, also suggest that these excitations are due to vHS's related to the nodal lines. As already mentioned above, a recent optical conductivity study of the nodal-line semimetal $BaNiS_2$ [35] showed spectral weight transfer from low to high energies via a temperature-independent isosbestic line, ending at a vHS, which was proposed to result from the connections between Dirac cones in the reciprocal space. Pronounced features in the optical conductivity spectra related to vHS's have also been observed in other Dirac materials, such as $ZrTe_5$ [6,40], $PbTe_2$ [8], T_d-$MoTe_2$ [41], and TaAs [42], and in the kagome metals Fe_3Sn_2 [7], $Co_3Sn_2S_2$ [32], and AV_3Sb_5 with A = K, Rb, Cs [43–45]. These vHS's may have different origin. In $ZrTe_5$, the quasidivergent peak observed in the optical conductivity was interpreted in terms of a vHS in the joint density of states. In AV_3Sb_5, they are due to band saddle points, while in Fe_3Sn_2 and $Co_3Sn_2S_2$ the observed sharp absorption peaks in the low-energy optical conductivity were attributed to the flat bands. In the case of the Dirac semimetal $PbTe_2$ the decrease and the collapse of the scattering rate of the low-energy charge carriers (i.e., the reduction in phase space for scattering) was interpreted as an experimental evidence for a vHS close to the Fermi level [8].

IV. CONCLUSION

In summary, we have performed a polarization-dependent in-plane infrared spectroscopy study of Nb_3SiTe_6 at low temperature, combined with DFT calculations of the electronic band structure and optical conductivity. The comparative experimental and theoretical study revealed a similar profile of the interband optical conductivity for both in-plane polarization directions, namely, several peaks due to interband transitions followed by a monotonic increase overlaid with various high-energy excitations. We found that the interband excitations along the c axis lead to pronounced and sharp peaks, in contrast to the less pronounced excitations for $\mathbf{E}\|a$, indicating an in-plane anisotropic behavior of Nb_3SiTe_6. Based on calculations of the band structure and optical conductivity, we assign the pronounced peaks at around 0.15 and 0.28 eV in the $\mathbf{E}\|c$ optical conductivity to van Hove singularities in the electronic density of states.

ACKNOWLEDGMENTS

C.A.K. acknowledges financial support by the Deutsche Forschungsgemeinschaft (DFG), Germany, through Grant No. KU 1432/15-1. Z.Q.M. acknowledges financial support by the US Department of Energy under Grant No. DE-SC0019068.

[1] J. Hu, X. Liu, C. L. Yue, J. Y. Liu, H. W. Zhu, J. B. He, J. Wei, Z. Q. Mao, L. Yu. Antipina, Z. I. Popov, P. B. Sorokin, T. J. Liu, P. W. Adams, S. M. A. Radmanesh, L. Spinu, H. Ji, and D. Natelson, Enhanced electron coherence in atomically thin Nb_3SiTe_6, Nat. Phys. **11**, 471 (2015).

[2] D. T. Son and B. Z. Spivak, Chiral anomaly and classical negative magnetoresistance of Weyl metals, Phys. Rev. B **88**, 104412 (2013).

[3] S.-S. Wang, Y. Liu, Z.-M. Yu, X.-L. Sheng, and S. A. Yang, Hourglass Dirac chain metal in rhenium dioxide, Nat. Commun. **8**, 1844 (2017).

[4] S. Li, Y. Liu, S.-S. Wang, Z.-M. Yu, S. Guan, X.-L. Sheng, Y. Yao, and S. A. Yang, Nonsymmorphic-symmetry-protected hourglass Dirac loop, nodal line, and Dirac point in bulk and monolayer X_3SiTe_6 (X = Ta, Nb), Phys. Rev. B **97**, 045131 (2018).

[5] R. Yu, Z. Fang, X. Dai, and H. Weng, Topological nodal line semimetals predicted from first-principles calculations, Front. Phys. **12**, 127202 (2017).

[6] R. Y. Chen, S. J. Zhang, J. A. Schneeloch, C. Zhang, Q. Li, G. D. Gu, and N. L. Wang, Optical spectroscopy study of the three-dimensional Dirac semimetal $ZrTe_5$, Phys. Rev. B **92**, 075107 (2015).

[7] A. Biswas, O. Iakutkina, Q. Wang, H. C. Lei, M. Dressel, and E. Uykur, Spin-Reorientation-Induced Band Gap in Fe_3Sn_2 : Optical Signatures of Weyl Nodes, Phys. Rev. Lett. **125**, 076403 (2020).

[8] E. van Heumen, M. Berben, L. Neubrand, and Y. Huang, Scattering rate collapse driven by a van Hove singularity in the Dirac semimetal $PdTe_2$, Phys. Rev. Mater. **3**, 114202 (2019).

[9] K. Kim, S. Kim, J. S. Kim, H. Kim, J.-H. Park, and B. I. Min, Importance of the van Hove singularity in superconducting $PdTe_2$, Phys. Rev. B **97**, 165102 (2018).

[10] M. Neupane, S.-Y. Xu, R. Sankar, Q. Gibson, Y. J. Wang, I. Belopolski, N. Alidoust, G. Bian, P. P. Shibayev, D. S. Sanchez, Y. Ohtsubo, A. Taleb-Ibrahimi, S. Basak, W.-F. Tsai, H. Lin, T. Durakiewicz, R. J. Cava, A. Bansil, F. C. Chou, and M. Z. Hasan, Topological phase diagram and saddle point singularity in a tunable topological crystalline insulator, Phys. Rev. B **92**, 075131 (2015).

[11] R. W. Havener, Y. Liang, L. Brown, L. Yang, and J. Park, Van hove singularities and excitonic effects in the optical conductivity of twisted bilayer graphene, Nano Lett. **14**, 3353 (2014).

[12] T. T. Heikkilä, N. B. Kopnin, and G. E. Volovik, Flat bands in topological media, JETP Lett. **94**, 233 (2011).

[13] T. Sato, Z. Wang, K. Nakayama, S. Souma, D. Takane, Y. Nakata, H. Iwasawa, C. Cacho, T. Kim, T. Takahashi, and Y. Ando, Observation of band crossings protected by nonsymmorphic symmetry in the layered ternary telluride Ta_3SiTe_6, Phys. Rev. B **98**, 121111(R) (2018).

[14] M. Naveed, F. Fei, H. Bu, X. Bo, S. A. Shah, B. Chen, Y. Zhang, Q. Liu, B. Wei, S. Zhang, J. Guo, C. Xi, A. Rahman, Z. Zhang, M. Zhang, X. Wan, and F. Song, Magneto-transport and Shubnikov-de Haas oscillations in the layered ternary telluride topological semimetal candidate Ta_3SiTe_6, Appl. Phys. Lett. **116**, 092402 (2020).

[15] C. Lee, H. Yan, L. E. Brus, T. F. Heinz, J. Hone, and S. Ryu, Anomalous lattice vibrations of single- and few-layer MoS_2, ACS Nano **4**, 2695 (2010).

[16] Z. Zhu, S. Li, M. Yang, X.-A. Nie, H.-K. Xu, X. Yang, D.-D. Guan, S. Wang, Y.-Y. Li, C. Liu, Z,-Q, Mao, N. Xu, Y. Yao, S. A. Yang, Y.-G. Shi, H. Zheng, and J.-F. Jia, A tunable and unidirectional one-dimensional electronic system $Nb_{2n+1}Si_nTe_{4n+2}$, npj Quantum Mater. **5**, 35 (2020).

[17] Y. Ohno, The scanning-tunneling microscopy, the x-ray photoelectron spectroscopy, the inner-shell-electron energy-loss spectroscopy studies of MTe_2 and M_3SiTe_6 (M= Nb and Ta), J. Solid State Chem. **142**, 63 (1999).

[18] L. An, H. Zhang, J. Hu, X. Zhu, W. Gao, J. Zhang, C. Xi, W. Ning, Z. Mao, and M. Tian, Magnetoresistance and Shubnikov–de Haas oscillations in layered Na_3SiTe_6 thin flakes, Phys. Rev. B **97**, 235133 (2018).

[19] Y. Pang, E. Rezaei, D. Chen, S. Li, Y. Jian, Q. Wang, Z. Wang, J. Duan, M. Zebarjadi, and Y. Yao, Thermoelectric properties of layered ternary telluride Na_3SiTe_6, Phys. Rev. Mater. **4**, 094205 (2020).

[20] J. Ebad-Allah, J. F. Afonso, M. Krottenmüller, J. Hu, Y. L. Zhu, Z. Q. Mao, J. Kuneš, and C. A. Kuntscher, Chemical pressure effect on the optical conductivity of the nodal-line semimetals ZrSiY (Y=S,Se,Te) and ZrGeY (Y=S,Te), Phys. Rev. B **99**, 125154 (2019).

[21] M. Köpf, J. Ebad-Allah, S. H. Lee, Z. Q. Mao, and C. A. Kuntscher, Influence of magnetic ordering on the optical response of the antiferromagnetic topological insulator $MnBi_2Te_4$, Phys. Rev. B **102**, 165139 (2020).

[22] J. Ebad-Allah, S. Rojewski, M. Vöst, G. Eickerling, W. Scherer, E. Uykur, Raman Sankar, L. Varrassi, C. Franchini, K.-H. Ahn, J. Kuneš, and C. A. Kuntscher, Pressure-Induced Excitations in the Out-of-Plane Optical Response of the Nodal-Line Semimetal ZrSiS, Phys. Rev. Lett. **127**, 076402 (2021).

[23] D. B. Tanner, Use of x-ray scattering functions in Kramers-Kronig analysis of reflectance, Phys. Rev. B **91**, 035123 (2015).

[24] P. Blaha, K. Schwarz, G. K. H. Madsen, D. Kvasnicka, J. Luitz, R. Laskowski, F. Tran, and L. D. Marks, *WIEN2K, An Augmented Plane Wave + Local Orbitals Program for Calculating Crystal Properties* (Karlheinz Schwarz, Techn. Universität Wien, Austria, 2018).

[25] P. Blaha, K. Schwarz, F. Tran, R. Laskowski, G. K. H. Madsen, and L. D. Marks, WIEN2k: An APW+lo program for calculating the properties of solids, J. Chem. Phys. **152**, 074101 (2020).

[26] J. P. Perdew, K. Burke, and M. Ernzerhof, Generalized Gradient Approximation Made Simple, Phys. Rev. Lett. **77**, 3865 (1996).

[27] J. Li, M. E. Badding, and F. J. DiSalve, Synthesis and structure of Nb_3SiTe_6, a new layered ternary niobium telluride compound, J. Alloys Compd. **184**, 257 (1992).

[28] C. Ambrosch-Draxl and J. O. Sofo, Linear optical properties of solids within the full-potential linearized augmented planewave method, Comput. Phys. Commun. **175**, 1 (2006).

[29] See Supplemental Material at http://link.aps.org/supplemental/10.1103/PhysRevB.107.115115 for further information on the experimental data and their analysis.

[30] A. Yaresko and A. V. Pronin, Low-Energy optical conductivity of TaP: comparison of theory and experiment, Crystals **11**, 567 (2021).

[31] I. Crassee, E. Martino, C. C. Homes, O. Caha, J. Novák, P. Tuückmantel, M. Hakl, A. Nateprov, E. Arushanov, Q. D. Gibson, R. J. Cava, S. M. Koohpayeh, K. E. Arpino, T. M. McQueen, M. Orlita, and Ana Akrap, Non-uniform carrier density in Cd_3As_2 evidenced by optical spectroscopy, Phys. Rev. B **97**, 125204 (2018).

[32] Y. Xu, J. Zhao, C. Yi, Q. Wang, Q. Yin, Y. Wang, L. Hu, L. Wang, E. Liu, G. Xu, L. Lu, A. A. Soluyanov, H. Lei, Y. Shi, J. Luo, and Z.-G. Chen, Electronic correlations and flattened band in magnetic Weyl semimetal candidate $Co_3Sn_2S_2$, Nat. Commun. **11**, 3985 (2020).

[33] Y. Shao, A. N. Rudenko, J. Hu, Z. Sun, Y. Zhu, S. Moon, A. J. Millis, S. Yuan, A. I. Lichtenstein, D. Smirnov, Z. Q. Mao, M. I. Katsnelson, and D. N. Basov, Electronic correlations in nodal-line semimetals, Nat. Phys. **16**, 636 (2020).

[34] B. Xu, L. X. Zhao, P. Marsik, E. Sheveleva, F. Lyzwa, Y. M. Dai, G. F. Chen, X. G. Qiu, and C. Bernhard, Temperature-Driven Topological Phase Transition and Intermediate Dirac Semimetal Phase in $ZrTe_5$, Phys. Rev. Lett. **121**, 187401 (2018).

[35] D. Santos-Cottin, M. Casula, L. de' Medici, F. Le Mardelé, J. Wyzula, M. Orlita, Y. Klein, A, Gauzzi, A. Akrap, and R. P. S. M. Lobo, Optical conductivity signatures of open Dirac nodal lines, Phys. Rev. B **104**, L201115 (2021).

[36] S. Ahn, E. J. Mele, and H. Min, Electrodynamics on Fermi Cyclides in Nodal Line Semimetals, Phys. Rev. Lett. **119**, 147402 (2017).

[37] Y. Shao, Z. Sun, Y. Wang, C. Xu, R. Sankar, A. J. Breidel, C. Cao, M. M. Fogler, A. J. Millis, F. Chou, Z. Li, T. Timusk, M. B. Maple, and D. N. Basov, Optical signatures of dirac nodal lines in $NbAs_2$, Proc. Natl. Acad. Sci. USA **116**, 1168 (2019).

[38] J. P. Carbotte, Optical response of a line node semimetal, J. Phys.: Condens. Matter **29**, 045301 (2017).

[39] S. P. Mukherjee and J. P. Carbotte, Transport and optics at the node in a nodal loop semimetal, Phys. Rev. B **95**, 214203 (2017).

[40] E. Martino, I. Crassee, G. Eguchi, D. Santos-Cottin, R. D. Zhong, G. D. Gu, H. Berger, Z. Rukelj, M. Orlita, C. C. Homes, and Ana Akrap, Two-Dimensional Conical Dispersion in $ZrTe_5$ Evidenced by Optical Spectroscopy, Phys. Rev. Lett. **122**, 217402 (2019).

[41] D. Santos-Cottin, E. Martino, F. Le Mardelé, C. Witteveen, F. O. von Rohr, C. C. Homes, Z. Rukelj, and Ana Akrap, Low-energy excitations in type-II Weyl semimetal T_d-$MoTe_2$ evidenced through optical conductivity, Phys. Rev. Mater. **4**, 021201(R) (2020).

[42] D. Santos-Cottin, J. Wyzula, F. Le Mardelé, I. Crassee, E. Martino, J. Novák, G. Eguchi, Z. Rukelj, M. Novak, M. Orlita, and Ana Akrap, Addressing shape and extent of Weyl cones in TaAs by Landau level spectroscopy, Phys. Rev. B **105**, L081114 (2022).

[43] E. Uykur, B. R. Ortiz, O. Iakutkina, M. Wenzel, S. D. Wilson, M. Dressel, and A. A. Tsirlin, Low-energy optical properties of the nonmagnetic kagome metal CsV_3Sb_5, Phys. Rev. B **104**, 045130 (2021).

[44] E. Uykur, B. R. Ortiz, S. D. Wilson, Martin Dressel, and Alexander A. Tsirlin, Optical detection of the density-wave instability in the kagome metal KV_3Sb_5, npj Quantum Mater. **7**, 16 (2022).

[45] M. Wenzel, B. R. Ortiz, S. D. Wilson, M. Dressel, A. A. Tsirlin, and E. Uykur, Optical study of RbV_3Sb_5: Multiple density-wave gaps and phonon anomalies, Phys. Rev. B **105**, 245123 (2022).